The Astrophysical Journal Letters, 858:L3 (8pp), 2018 May 1 https://doi.org/10.3847/2041-8213/aabde9

Quasi-periodic Pulsations in the Most Powerful Solar Flare of Cycle 24

Dmitrii Y. Kolotkov[1], Chloe E. Pugh[1], Anne-Marie Broomhall[1,2], and Valery M. Nakariakov[1,3]
[1] Centre for Fusion, Space and Astrophysics, Department of Physics, University of Warwick, Coventry CV4 7AL, UK; D.Kolotkov@warwick.ac.uk, D.Kolotkov.1@warwick.ac.uk
[2] Institute of Advanced Study, University of Warwick, Coventry CV4 7HS, UK
[3] St. Petersburg Branch, Special Astrophysical Observatory, Russian Academy of Sciences, 196140, St. Petersburg, Russia
Received 2018 March 7; revised 2018 April 12; accepted 2018 April 12; published 2018 April 26

Abstract

Quasi-periodic pulsations (QPPs) are common in solar flares and are now regularly observed in stellar flares. We present the detection of two different types of QPP signals in the thermal emission light curves of the X9.3-class solar flare SOL2017-09-06T12:02, which is the most powerful flare of Cycle 24. The period of the shorter-period QPP drifts from about 12 to 25 s during the flare. The observed properties of this QPP are consistent with a sausage oscillation of a plasma loop in the flaring active region. The period of the longer-period QPP is about 4 to 5 minutes. Its properties are compatible with standing slow magnetoacoustic oscillations, which are often detected in coronal loops. For both QPP signals, other mechanisms such as repetitive reconnection cannot be ruled out, however. The studied solar flare has an energy in the realm of observed stellar flares, and the fact that there is evidence of a short-period QPP signal typical of solar flares along with a long-period QPP signal more typical of stellar flares suggests that the different ranges of QPP periods typically observed in solar and stellar flares is likely due to observational constraints, and that similar physical processes may be occurring in solar and stellar flares.

Key words: Sun: flares – Sun: oscillations – Sun: UV radiation – Sun: X-rays, gamma rays

1. Introduction

The X9.3-class solar flare that occurred on 2017 September 6 is the most powerful since 2005, and hence is the largest flare observed with the latest generation of instruments and in Cycle 24. Using the relationship between the *Geostationary Operational Environmental Satellite*'s (*GOES*) soft X-ray flux in the 1–8 Å waveband and the flare energy calculated from the total solar irradiance found by Kretzschmar (2011), X9.3 class corresponds to an energy of around 10^{32} erg. The energy of this flare is therefore in the realm of typically observed stellar flare energies, and solar flares such as this are useful for bridging the energy gap between solar and stellar flares (Maehara et al. 2015).

Quasi-periodic pulsations (QPPs) are a common feature of solar flares, detected in all observational wavebands, from radio to gamma-rays, in all phases of the flare (see Inglis et al. 2016; Pugh et al. 2017b for recent comprehensive statistical studies), and in both thermal and nonthermal emissions (see Kupriyanova et al. 2010; Simões et al. 2013, respectively). QPPs are a transient phenomenon, hence they tend to be seen in part of the flare light curve, rather than being seen throughout the whole flare. The specific values of QPP periods range from a fraction of a second to several tens of minutes (e.g., Nakariakov et al. 2016; Van Doorsselaere et al. 2016), and hence are likely to be associated with several different physical mechanisms (see McLaughlin et al. 2018 for a recent review). It has been established that QPPs could be caused by several groups of mechanisms, including MHD-wave-driven and spontaneous magnetic reconnection. Revealing these mechanisms is still an active research area.

QPPs are also detected in stellar flares in the same observational channels as solar flares (e.g., Mitra-Kraev et al. 2005; Pandey & Srivastava 2009; Srivastava et al. 2013; Cho et al. 2016 for X-rays; and, e.g., Gudel et al. 1989; Zaitsev et al. 2004 for radio). Stellar QPPs are usually detected in flares on active red dwarfs, but are also observed on Sun-like stars. In addition, QPPs are detected in stellar flares in the white light (WL) emission (e.g., Mathioudakis et al. 2003; Anfinogentov et al. 2013). A recent statistical study demonstrated that a significant fraction of WL flares detected with *Kepler* have QPPs (Pugh et al. 2016).

The WL stellar flares have recently attracted major attention in the context of devastating superflares that can strongly affect the habitability of the planets orbiting a flaring star. There naturally appears a question of whether or not the Sun is capable of producing a superflare, and if so what the superflare occurrence rate is (e.g., Maehara et al. 2012; Namekata et al. 2017; Tschernitz et al. 2018). In solar flares, the enhancement of the WL emission is usually very weak, with values typically less than 0.01% of the total irradiance. In contrast, in strong stellar WL flares the increase in the star's irradiance is comparable to its irradiance in the quiet period. Moreover, some stellar WL flares do not have a significant X-ray flux (e.g., Haisch et al. 1991). Thus, it is not clear whether stellar WL superflares and solar flares are produced by the same physical mechanisms, and whether the results of stellar flare studies could be scaled down to the Sun. The detection of QPPs in stellar WL flares with properties similar to those of QPPs in solar flares, in particular with damping patterns (Cho et al. 2016; Pugh et al. 2016) and multiple periods (Pugh et al. 2015; Doyle et al. 2018), suggests that the mechanisms could be the same.

So far, the most powerful solar flare with a QPP pattern detected is an X14.4 flare (Mészárosová et al. 2006). The flare had QPPs with periods ranging from 1 to 5 minutes, detected in the radio and hard X-ray emission. In this Letter, we present the second most powerful solar flare with detected QPPs, which is the most powerful flare of Cycle 24. The Letter is organized as follows: observations used for the analysis are described in Section 2, Section 3 gives a methodology used for processing the observational time series, the obtained results are summarized in Section 4 and discussed in Section 5.

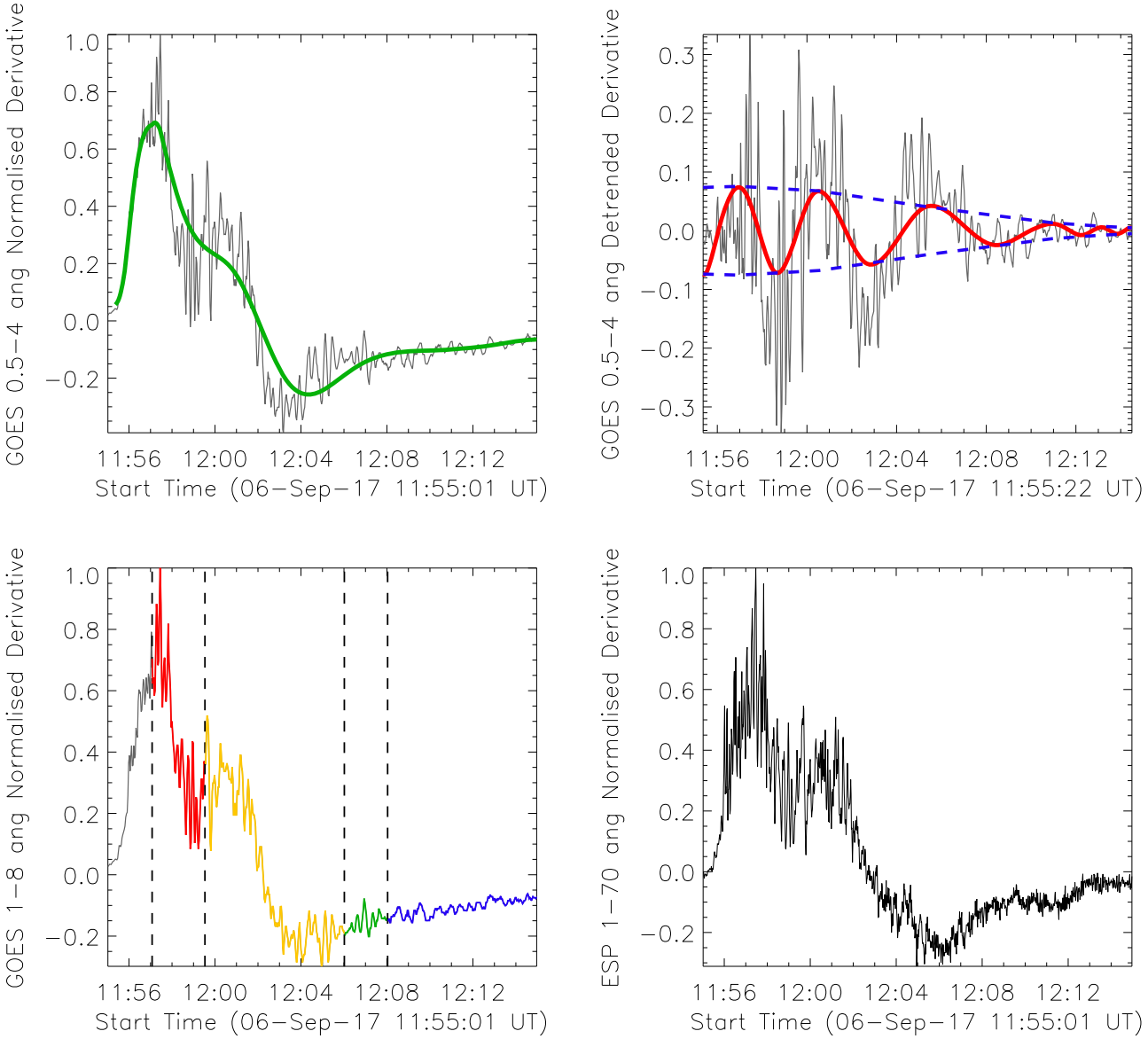

Figure 1. Time derivatives of the fluxes measured by *GOES*/XRS (left panels) and *SDO*/EVE/ESP (bottom right) during the impulsive phase of the flare, normalized to their maximum value. The green line in the top left panel shows an overall trend of the 0.5–4 Å signal, detected with the empirical mode decomposition (EMD) method. The top right panel shows the signal with the overall trend subtracted, and an intrinsic mode (the red line) found to be statistically significant in the detrended signal by EMD (see Figure 2). The blue dashed lines show a Gaussian envelope of the intrinsic mode (see Section 4 for details). Different colors in the bottom left panel illustrate the sections of the light curve, used for further analyses (see Figures 3 and 4 and Table 1).

2. Observations

The flare analyzed in this Letter occurred on 2017 September 6 and peaked at 12:02:00 UT. It originated from the active region NOAA 12673 and is the most powerful flare of Cycle 24.

In this study, we used data from two instruments that observed the flare (see Figure 1), which are the *GOES* X-ray sensor (XRS) and the Extreme ultraviolet SpectroPhotometer (ESP) channel of the Extreme ultraviolet Variability Experiment (EVE) on board the *Solar Dynamics Observatory* (*SDO*). *GOES*/XRS makes Sun-as-a-star observations of soft X-ray flux in the 1–8 Å and 0.5–4 Å wavebands with a cadence of 2.048 s, while EVE/ESP covers 1–70 Å wavelengths with a cadence of 0.25 s. The uncertainties on the XRS and ESP data were estimated using the same approach as Pugh et al. (2017b).

3. Data Analysis

3.1. Periodogram-based Analysis

Stationary QPPs, i.e., those with constant periods, were studied with the analysis technique described in detail in Pugh et al. (2017a), which is based upon the work of Vaughan (2005) and is outlined below. The technique assesses the statistical significance of peaks in a periodogram, accounting for both data uncertainties and colored noise, which results in the Fourier power spectral density S and the frequency f being connected as

$$S \propto f^{-\alpha}, \quad (1)$$

where the power-law index α determines the "color" of noise.

In addition to the analysis of the entire flare light curves as shown in Figures 1 and 2, the light curves were manually trimmed to focus on shorter time intervals that were treated

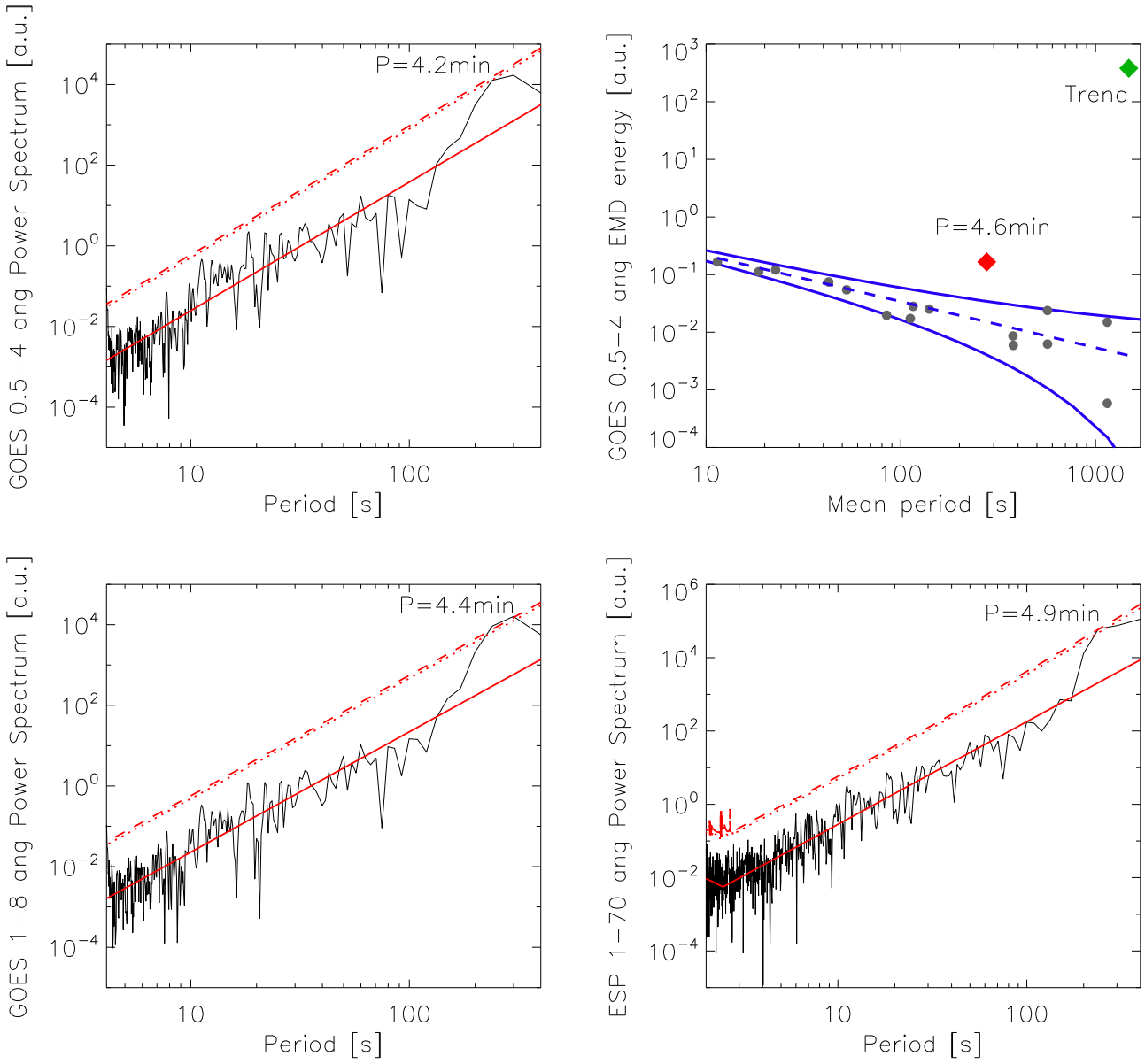

Figure 2. Periodograms of the *GOES*/XRS (top left and bottom left) and *SDO*/EVE/ESP (bottom right) signals shown in Figure 1, where the red solid lines are broken power-law fits to the spectra, and the red dotted and dashed lines represent the 95% and 99% confidence levels, respectively. Top right: EMD spectrum, i.e., the dependence of the total energy of an intrinsic mode upon the mean period, in the detrended 0.5–4 Å signal (see Figure 1). The blue solid lines show the limits of the 99% confidence interval, inside which the modes belong to noise. The mean energy is determined by Equation (2) and is shown by the blue dashed line. The intrinsic modes associated with noise are shown by the black circles; the mode with statistically significant properties and flare trend are shown by the red and green diamonds, respectively.

separately as potentially containing QPP signals (see Figures 1, 3, and 4). Periodograms were then calculated separately for each of the light curve sections, and a broken power-law model was fitted to the resulting periodograms. The model uncertainties at each frequency bin were then factored into the calculation of the 95% and 99% significance levels in the manner described by Pugh et al. (2017a, 2017b).

The start and end times of the signal were altered by cutting off or adding individual data points to maximize the height of any peak in the periodogram that could correspond to a potential QPP signal. The combination producing the maximum signal-to-noise ratio was kept. This process is necessary since the signals can be short-lived, meaning that even minor changes to the length of the data can affect the signal-to-noise ratio. Changing the length of the data included in the analysis also changes the resolution of the frequency bins, preventing the case where the signal, by chance, lies between two sampled frequencies.

For the final step prior to calculating the periodogram, the start and end values of these multiple flare sections were equalized to each other by subtracting a linear interpolation between them. Since calculating the periodogram assumes that the time series data is cyclic, doing this removes the apparent discontinuity between the start and end times that can introduce false signal into the power spectrum. The subtraction of a linear trend in the time domain does not alter the probability distribution of values in the power spectrum, hence it is compatible with the significance testing method used in this Letter.

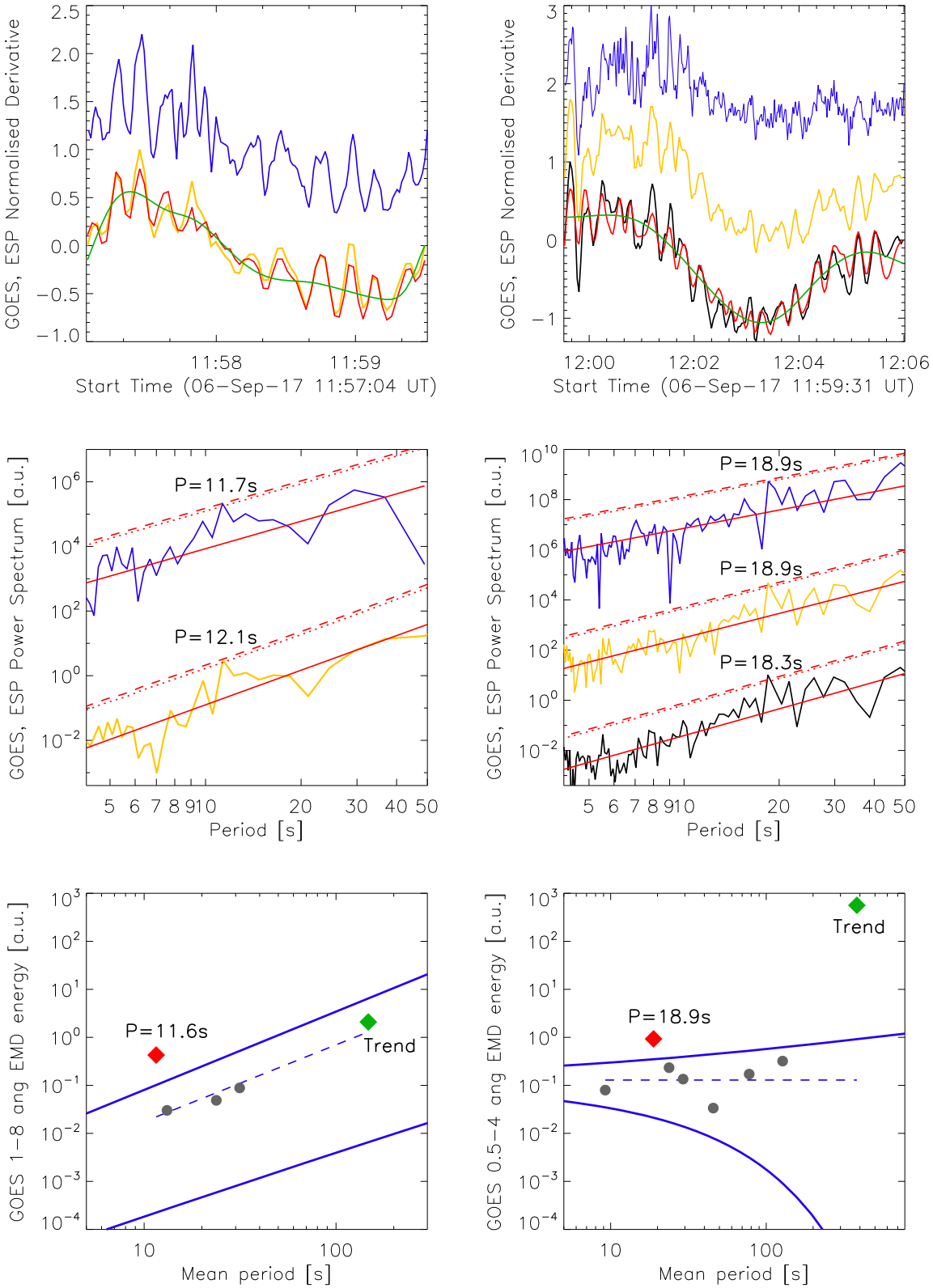

Figure 3. Similar to Figures 1 and 2, but for the flare sections, starting from 11:57:04 UT (left) and 11:59:31 UT (right), and with a linear interpolation between the start and end values subtracted (see Section 3.1 for details). Only those light curves with a significant QPP signal are included in these plots. Signals at 1–8 Å, 0.5–4 Å, and 1–70 Å wavebands and their power spectra are shown in the top and middle panels by the yellow, black, and blue lines, respectively. The green and red lines in the top panels show the overall trends and significant oscillations detected in the corresponding signals with EMD, respectively. All the curves in the top and middle panels were normalized to their maximum values and shifted upward or downward for a better visualization. Bottom panels show the EMD spectra of 1–8 Å (left) and 0.5–4 Å (right) signals. The notations are similar to those in Figure 2.

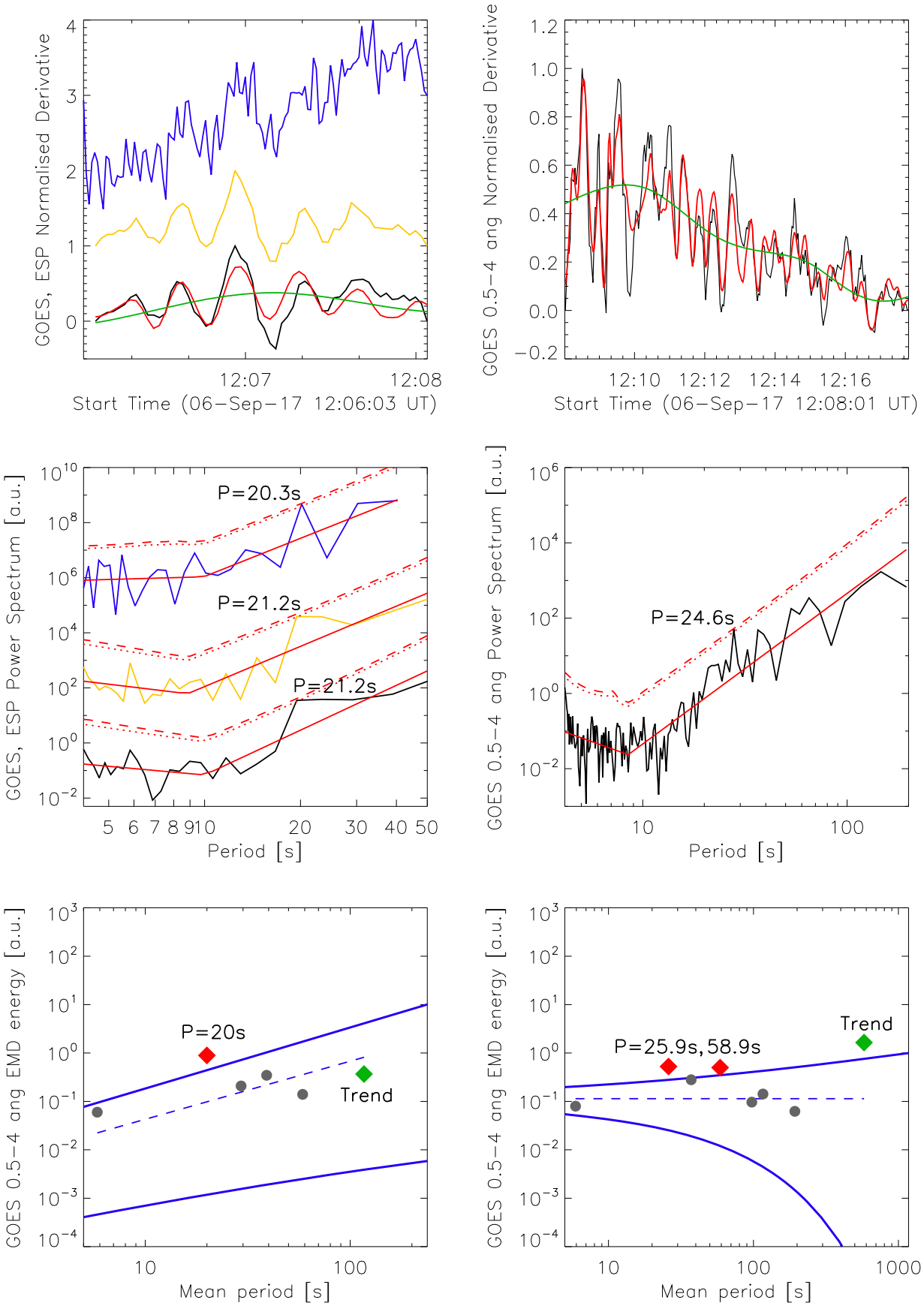

Figure 4. Similar to Figure 3, but for the flare sections, starting from 12:06:03 UT (left) and 12:08:01 UT (right). The red line in the top right panel shows a superposition of the two modes found to be significant in the EMD spectrum.

Table 1
Statistically Significant Periods Detected above 95% Significance Level (Except where Indicated) in the Signals Shown in Figures 1, 3, and 4, with the Periodogram and EMD Methods

Start Time (UTC)	End Time (UTC)	QPP Duration (s)	1–8 Å Period (s) Periodogram/EMD	0.5–4 Å Period (s) Periodogram/EMD	1–70 Å Period (s) Periodogram
11:55:01	12:14:58	1197	265^{+83}_{-63}	254^{+71}_{-55}(94%)/276^{+43}_{-81}	293^{+102}_{-76}
11:57:04	11:59:31	147	$12.1^{+1.4}_{-1.3}$/$11.6^{+2.7}_{-2.0}$	⋯	$11.7^{+2.3}_{-1.9}$
11:59:31	12:06:01	390	$18.9^{+0.2}_{-0.2}$	$18.3^{+4.8}_{-3.8}$/$18.9^{+5.3}_{-3.9}$	$18.9^{+0.2}_{-0.2}$
12:06:03	12:08:04	121	$21.2^{+0.8}_{-0.8}$	$21.2^{+0.8}_{-0.8}$/$20.0^{+3.5}_{-2.6}$	$20.3^{+0.4}_{-0.4}$
12:08:01	12:17:48	587	⋯	$24.6^{+4.0}_{-3.4}$/$25.9^{+5.3}_{-6.3}$, $58.9^{+11.5}_{-9.4}$	⋯

Note. The periodogram and EMD results are separated by a forward slash ("/"). When only one value appears, it was determined from the periodogram.

3.1.1. Time Derivative Data

As shown by previous studies, QPPs can be more easily detected in the time derivative of soft X-ray (SXR) observations than in the raw observations themselves (e.g., Simões et al. 2015; Hayes et al. 2016; Dennis et al. 2017). This is because the change in SXR flux during the impulsive phase of a flare, where QPPs are predominantly observed, is often vastly greater in amplitude than the QPP being searched for. Since taking the derivative can be thought of as a form of detrending, its impact is also taken into account. Pugh et al. (2017b) demonstrated how taking a three-point finite difference approximation to the derivative of time series data alters the power spectrum. Namely, a $\sin^2\omega$ multiplying term is introduced to the power spectrum, where ω is an angular frequency varying between 0 and π at the lowest and highest frequencies, respectively. This means that the periodogram approaches zero toward these frequencies. Therefore, the first and final two frequency bins had to be removed from the analysis. Based on this, the power spectra shown in Figures 2–4 were divided by the $\sin^2\omega$ term before the confidence limits were calculated.

3.2. Empirical Mode Decomposition (EMD) Analysis

Operating locally and not being restricted by the basis of expansion (see Huang et al. 1998; Huang & Wu 2008), EMD is found to be naturally suitable for processing QPPs in solar and stellar flares (see, e.g., Nakariakov et al. 2010; Kolotkov et al. 2015; Cho et al. 2016; Doyle et al. 2018), including non-stationary QPPs with a strong period drift (see those studied by Kupriyanova et al. 2010). By the full analogy with the periodogram approach, where significance of the detected spectral components can be tested by the method discussed in Section 3.1, not all EMD modes necessarily correspond to statistically significant oscillatory processes. The latter must be checked with a similar significance test and taken as an intrinsic and compulsory feature of the method. The statistics of power-law distributed processes, including random noise as a specific case, was incorporated in the EMD analysis by Wu & Huang (2004) and Kolotkov et al. (2016), and this is briefly outlined here. In this study, we treat the observational signal as a superposition of a smooth slowly varying trend (the flare itself), a possible oscillation that can be modulated by amplitude, period, and phase, and colored noise characterized by the same power-law index α, as introduced in Section 3.1. In the parlance of the EMD analysis, the dependence of the total energy E_m of intrinsic modes upon the period P_m in pure colored noise is given by

$$E_m P_m^{1-\alpha} = \text{const}, \quad (2)$$

which is similar to Equation (1) describing behavior of colored noise in the Fourier power spectrum.

Having obtained the dependence of the total energy of identified intrinsic modes upon their mean period, which may be referred to as an EMD spectrum (see Figures 2–4), one can estimate the value of the power-law index α, i.e., the color of noise superimposed on the initial observational signal, by approximation a functional form of Equation (2) into this spectrum. The very last mode of the expansion, showing an overall trend of the signal, is usually excluded from this approximation, corresponding to an effective and self-consistent detrending of the original light curve. Furthermore, given the definition of the total energy of an intrinsic mode as a sum of squares of its instantaneous amplitudes, it is therefore chi-squared distributed at each instantaneous period in the EMD spectrum. The parameter of the distribution function, the number of degrees of freedom, varies with the period and the color of noise considered (see Kolotkov et al. 2016 for details). This distribution can be visualized via the confidence interval of, e.g., 99% significance in the EMD spectrum. Thus, the modes whose energies lie off this interval should be treated as statistically significant, while the modes within this interval are indistinguishable from the background processes governed by the power law with a certain value of the index α, i.e., colored noise.

In this study, we applied the described methodology to both the full flare light curve, as shown in Figures 1 and 2, and to those trimmed sections of the flare that show the highest signal-to-noise ratio of spectral peaks in the periodogram-based analysis (see Figures 3 and 4), focusing on the *GOES* data only.

4. Results

The oscillation periods found to be statistically significant by the periodogram and EMD analyses in the full and trimmed flare light curves are summarized in Table 1. They can be attributed to two different types of QPPs observed simultaneously in this flare: those with a non-stationary short period drifting from about 12 to 25 s, and the other with a much longer period varying from about 4 to 5 minutes in different observational wavebands. In addition, EMD detected a 1 minute oscillation pronounced from 12:08:01 to 12:17:48 UT (a post-flare phase), which is not found to be significant using the periodogram-based technique.

The evidence of the longer-period variability is shown in Figure 2 by both the periodograms and EMD spectrum, with

confidence above 95%. It is detected in both the *GOES*/XRS and *SDO*/EVE/ESP observations, and at all analyzed wavebands. Its behavior in the time domain is shown in Figure 1. It represents a rapidly decaying oscillation with a harmonic shape and a relatively stable period of about 4 to 5 minutes. The top right panel of Figure 1 appears to show that the oscillation is modulated by a Gaussian envelope, which was found to be substantially better than an exponential form, with a damping time of about 7.5 minutes. This value gives an oscillation quality factor (defined as the ratio of the damping time to the period) of about 1.6.

The spectra of the shorter flare sections containing statistically significant oscillatory components and their corresponding time series are shown in Figures 3 and 4. Their oscillation periods are found to be similar by both the periodogram and EMD analyses, and gradually increase with the progression of the flare from about 12 s at the flare maximum to about 25 s in the flare decay phase (see Table 1). Unlike the longer-period variation described above, the detected shorter-period oscillations have a rather intermittent, wave-train-like, amplitude modulation, with the oscillation power highly localized in time (see, e.g., the oscillation profile found in the time interval from 12:06:03 to 12:08:04 UT). In addition, EMD detected a 1 minute oscillation in the decay phase section starting from 12:08:01 UT, with the confidence above the 99% level. It is shown in combination with the 25 s component and a low-frequency trend in Figure 4, and has a similar amplitude modulated behavior.

5. Discussion and Conclusions

Our study demonstrates the presence of at least two QPPs in an X9.3 flare. In contrast with the QPP detection in an X14.4 flare by Mészárosová et al. (2006), the detected QPPs occur in the thermal emission. The observed values of the longer oscillation period (4–5 minutes) and quality factor (1.6) are consistent with those typically detected in so-called SUMER oscillations (e.g., Wang 2011) that are usually interpreted as slow magnetoacoustic oscillations in flaring loops. Similar values were found in soft X-ray intensity QPPs in both stellar and less powerful solar flares (Cho et al. 2016). In addition, the Gaussian damping is similar to the decaying oscillatory patterns in stellar flares observed in WL (Pugh et al. 2016). The observed period, quality factor, and the fact that the thermal emission is modulated suggest that a possible mechanism for this QPP is a standing slow magnetoacoustic oscillation in the site of the analyzed flare (see the results of the numerical modeling by, e.g., Selwa et al. 2005; Taroyan et al. 2007). However, we cannot rule out the possibility that the QPPs are associated with other mechanisms, such as repetitive reconnection.

The other period, 12–25 s, is in the range of the most common QPPs detected in solar flares (see Inglis et al. 2016; McLaughlin et al. 2018). QPPs with periods in this range are usually interpreted as being associated with standing sausage oscillations of coronal loops. The period of this oscillation mode is determined by the parallel or perpendicular Alfvén transit time in the oscillating plasma structure in the trapped (e.g., Zaitsev & Stepanov 1982; Roberts et al. 1984) and leaky regimes (e.g., Cally 1986; Kopylova et al. 2007; Nakariakov et al. 2012), respectively. In this interpretation, the observed gradual increase of the oscillation period could be readily attributed to the gradual evolution of the physical parameters in the oscillating loop, for example, the increase in loop length (Hayes et al. 2016), and/or the increase in plasma density because of the evaporation upflows. The detection of this kind of QPP in such an energetic solar flare suggests that similar QPPs could be found in stellar flares too.

The simultaneous occurrence of QPPs with periods of several minutes and a few tens of seconds in an X9.3 solar flare further strengthens the conclusion that QPPs are a common feature of powerful energy releases. Although solar QPP periods can range from subseconds to over a minute, the shorter period observed here is similar to the periods detected in many solar flares (e.g., recent surveys by Inglis et al. 2016; Pugh et al. 2017b). The longer-period QPP has a period similar to the majority of those detected in stellar flares (e.g., Cho et al. 2016; Pugh et al. 2016). This apparent difference between solar and stellar QPP periods is probably artificial, likely being due to a selection bias because we only tend to observe the more energetic, longer-lasting stellar flares and, importantly, the observational time resolution of stellar light curves is often coarser. Furthermore, many typical solar flares have shorter lifetimes, prohibiting the detection of longer-period QPPs. Here, the detection of the longer-period QPP is only possible because the flare is unusually energetic and long-lived. The simultaneous detection of the two distinct QPP timescales in a powerful solar flare, whose energy is comparable to that of stellar flares, indicates that the longer- and shorter-period QPP regimes are not mutually exclusive, which could therefore indicate the similarity of physical mechanisms responsible for the energy releases on the Sun and stars.

A.M.B., D.Y.K., and V.M.N. acknowledge the support of the STFC consolidated grant ST/P000320/1. This work was supported in part by the Russian Foundation for Basic Research grant No. 17-52-80064 (V.M.N.). We also acknowledge support from the International Space Science Institute for the team "Quasi-periodic Pulsations in Stellar Flares: a Tool for Studying the Solar-Stellar Connection."

ORCID iDs

Dmitrii Y. Kolotkov https://orcid.org/0000-0002-0687-6172
Chloe E. Pugh https://orcid.org/0000-0003-2516-2164
Anne-Marie Broomhall https://orcid.org/0000-0002-5209-9378
Valery M. Nakariakov https://orcid.org/0000-0001-6423-8286

References

Anfinogentov, S., Nakariakov, V. M., Mathioudakis, M., van Doorsselaere, T., & Kowalski, A. F. 2013, ApJ, 773, 156
Cally, P. S. 1986, SoPh, 103, 277
Cho, I.-H., Cho, K.-S., Nakariakov, V. M., Kim, S., & Kumar, P. 2016, ApJ, 830, 110
Dennis, B. R., Tolbert, A. K., Inglis, A., et al. 2017, ApJ, 836, 84
Doyle, J., Shetye, J., Antonova, A., et al. 2018, MNRAS, 475, 2842
Gudel, M., Benz, A. O., Bastian, T. S., et al. 1989, A&A, 220, L5
Haisch, B., Strong, K. T., & Rodono, M. 1991, ARA&A, 29, 275
Hayes, L. A., Gallagher, P. T., Dennis, B. R., et al. 2016, ApJL, 827, L30
Huang, N. E., Shen, Z., Long, S. R., et al. 1998, RSPSA, 454, 903
Huang, N. E., & Wu, Z. 2008, RvGeo, 46, RG2006
Inglis, A. R., Ireland, J., Dennis, B. R., Hayes, L., & Gallagher, P. 2016, ApJ, 833, 284
Kolotkov, D. Y., Anfinogentov, S. A., & Nakariakov, V. M. 2016, A&A, 592, A153

Kolotkov, D. Y., Nakariakov, V. M., Kupriyanova, E. G., Ratcliffe, H., & Shibasaki, K. 2015, A&A, 574, A53
Kopylova, Y. G., Melnikov, A. V., Stepanov, A. V., Tsap, Y. T., & Goldvarg, T. B. 2007, AstL, 33, 706
Kretzschmar, M. 2011, A&A, 530, A84
Kupriyanova, E. G., Melnikov, V. F., Nakariakov, V. M., & Shibasaki, K. 2010, SoPh, 267, 329
Maehara, H., Shibayama, T., Notsu, S., et al. 2012, Natur, 485, 478
Maehara, H., Shibayama, T., Notsu, Y., et al. 2015, EP&S, 67, 59
Mathioudakis, M., Seiradakis, J. H., Williams, D. R., et al. 2003, A&A, 403, 1101
McLaughlin, J. A., Nakariakov, V. M., Dominique, M., Jelínek, P., & Takasao, S. 2018, SSRv, 214, 45
Mészárosová, H., Karlický, M., Rybák, J., Fárník, F., & Jiřička, K. 2006, A&A, 460, 865
Mitra-Kraev, U., Harra, L. K., Williams, D. R., & Kraev, E. 2005, A&A, 436, 1041
Nakariakov, V. M., Hornsey, C., & Melnikov, V. F. 2012, ApJ, 761, 134
Nakariakov, V. M., Inglis, A. R., Zimovets, I. V., et al. 2010, PPCF, 52, 124009
Nakariakov, V. M., Pilipenko, V., Heilig, B., et al. 2016, SSRv, 200, 75
Namekata, K., Sakaue, T., Watanabe, K., et al. 2017, ApJ, 851, 91
Pandey, J. C., & Srivastava, A. K. 2009, ApJL, 697, L153
Pugh, C. E., Armstrong, D. J., Nakariakov, V. M., & Broomhall, A.-M. 2016, MNRAS, 459, 3659
Pugh, C. E., Broomhall, A.-M., & Nakariakov, V. M. 2017a, A&A, 602, A47
Pugh, C. E., Nakariakov, V. M., & Broomhall, A.-M. 2015, ApJL, 813, L5
Pugh, C. E., Nakariakov, V. M., Broomhall, A.-M., Bogomolov, A. V., & Myagkova, I. N. 2017b, A&A, 608, A101
Roberts, B., Edwin, P. M., & Benz, A. O. 1984, ApJ, 279, 857
Selwa, M., Murawski, K., & Solanki, S. K. 2005, A&A, 436, 701
Simões, P. J. A., Fletcher, L., Hudson, H. S., & Russell, A. J. B. 2013, ApJ, 777, 152
Simões, P. J. A., Hudson, H. S., & Fletcher, L. 2015, SoPh, 290, 3625
Srivastava, A. K., Lalitha, S., & Pandey, J. C. 2013, ApJL, 778, L28
Taroyan, Y., Erdélyi, R., Wang, T. J., & Bradshaw, S. J. 2007, ApJL, 659, L173
Tschernitz, J., Veronig, A. M., Thalmann, J. K., Hinterreiter, J., & Pötzi, W. 2018, ApJ, 853, 41
Van Doorsselaere, T., Kupriyanova, E. G., & Yuan, D. 2016, SoPh, 291, 3143
Van Doorsselaere, T., Shariati, H., & Debosscher, J. 2017, ApJS, 232, 26
Vaughan, S. 2005, A&A, 431, 391
Wang, T. 2011, SSRv, 158, 397
Wu, Z., & Huang, N. E. 2004, RSPSA, 460, 1597
Zaitsev, V. V., Kislyakov, A. G., Stepanov, A. V., Kliem, B., & Furst, E. 2004, AstL, 30, 319
Zaitsev, V. V., & Stepanov, A. V. 1982, SvA, 26, 340